Journal of Marine Science and Application (2025) 24: 176-193
https://doi.org/10.1007/s11804-024-00431-4

RESEARCH ARTICLE

Hydrodynamic Performance of Two Types of Floating Breakwaters Integrated With a Wave Energy Converter

Qiaoling Ji[1,2], Guoqiang Chen[1], Yan Xu[1] and Sheng Dong[3]

Received: 22 June 2023 / Accepted: 28 August 2023

Abstract

Two asymmetric types of floating breakwaters integrated with a wave energy converter (WEC-FBs), a floating square box with a triangle (trapezoidal type) or a wave baffle (L type) attached to its rear side, have been proposed. In this research, the hydrodynamic performance, including capture width ratio (CWR), wave transmission coefficient, heave motion, and force coefficient, were studied and compared between the two types. A numerical simulation model based on the Navier–Stokes equation was employed. The effects of power take-off (PTO) damping coefficient, wave periods, and draft/displacement on the hydrodynamic performance of the two structure shapes were simulated and investigated. The results reveal that the L type performs better in shorter wave periods, and the trapezoidal type exhibits a higher CWR in intermediate wave periods. This study offers knowledge of the design and protection of the two WEC-FB types.

Keywords Floating breakwater; Wave energy converter; Hydrodynamic performance; Capture width ratio; Transmission coefficient; CFD simulation

1 Introduction

Wave energy is a renewable and clean source of energy that has a considerable storage capacity as well as high energy density. The point absorber type, which oscillates in a vertical direction to generate energy, constitutes most (more than 81%) of the WECs. However, WEC systems still suffer from high costs. Integrating WECs into other maritime structures is another way to increase their attractiveness. Floating breakwaters (FBs), for the similarity in environmental conditions and structural configurations, have been promoted to combine with point absorber WECs as WEC-FB integrations. A comprehensive review of the research and development of WEC-FBs was presented by Zhao et al. (2019).

Buoy geometry is a major parameter affecting WEC-FB efficiency (Zhang et al., 2016; Chen et al., 2020). Madhi et al. (2014) proposed an asymmetric heaving WEC-FB (the Berkeley wedge), with one side smoothly curved and the other side a needle-like vertical face, to minimize the influence of viscosity. In another method, the WEC is deployed as a separate unit on the seaward side of the breakwater (Reabroy et al., 2019; Zhang et al., 2021).

Using a 2D frequency-domain semi-analytical model, Zhou et al. (2022) found that among six geometries, the bottom of triangular and reversed circular arcs could improve the hydrodynamic performance of WEC-FBs. Notably, for nonuniform cross sections such as a cone, nonlinear viscous effects are important even for small and flat waves (Jin et al. 2019; Berenjkoob et al., 2021). Zhang et al. (2020) studied three asymmetric WEC-FBs, including a triangle and a triangle-baffle at the bottom as an additional screening structure, which substantially improved the performance of wave resistance and energy capture, almost equaling the Berkeley-wedge type. This asymmetric trapezoidal type was also studied by Wan et al. (2023) in an OB-OWC-WEC system comprising a cylindrical caisson

Article Highlights

- Two asymmetric types of WEC-FBs, trapezoid type and L type, are studied and compared.
- The effects of PTO damping coefficient, wave periods, and draft/displacement are analyzed.
- Two force parameters are introduced as a criterion for geometry optimization.
- The two types of floating breakwaters are suitable for a certain range of wave periods.

✉ Sheng Dong
dongsh@ouc.edu.cn

[1] College of Transportation, Shandong University of Science and Technology, Qingdao 266590, China

[2] Shandong Key Laboratory of Civil Engineering Disaster Prevention and Mitigation, Qingdao 266590, China

[3] College of Engineering, Ocean University of China, Qingdao 266404, China

breakwater acting as an Oscillating Water Column (OWC) with an OB hinged in front of the OWC. They obtained the same conclusion as Zhang et al. (2020) through comparison with the Berkeley wedge and other shapes. These studies demonstrated that an asymmetric geometric shape with an extra structure attached at the rear side helps improve the hydrodynamic performance of the WEC-FB to a large extent.

The shapes resulting from these geometry optimization studies can be quite complicated to manufacture. Therefore, shapes with suboptimal hydrodynamic performance but low manufacturing cost should also be included to provide diverse feasible solutions in practical engineering (Garcia-Teruel and Forehand, 2022). In contrast, curtain-wall-type breakwaters have been widely used in coastal protection engineering for many years (Haren, 1979). Using a semi-analytical method, Deng et al. (2021) found that the added mass could achieve the maximum when an attached vertical plate was installed at the ends of the upper box. On this basis, Ji et al. (2021) proposed a reversed L type WEC-FB with a wave baffle attached to a box at its rear side. Their results showed that its energy capture ratio for a vorticity eddy is considerably improved over that of the box type but quite smaller than that of the Berkeley wedge type because of straight corners. Moreover, the two parts of this geometry type can be prefabricated and installed separately, thus simplifying the manufacturing construction process and saving costs.

In the above studies, the comparison of buoy shapes focused on a similar type to find the geometry for the best hydrodynamic performance. For these diverse geometries, the hydrodynamics was investigated for different aims and in different conditions in different studies. The present study compares the hydrodynamic and energy capture performances of two asymmetric types of WEC-FBs in identical conditions. One is the widely optimized trapezoidal type with a triangular bottom, the other is an L type with a curtain wall as a wave baffle. The purpose of the study is not to optimize the best shape but to provide a useful reference for practical design and application.

The remainder of this paper is organized as follows. In Section 2, a Volume of Fluid-based Computational Fluid Dynamics (VOF-based CFD) with a coupled fluid solver and motion solver is introduced. In Section 3, a numerical wave tan with a WEC-FB model installed is established, the reliabilities of which in wave generation, grid convergence, and wave–structure interaction simulation are validated by the corresponding experimental data. In Section 4, the effects of the PTO damping coefficient, environmental conditions, and the geometric parameters of the draft and displacement of WEC-FBs on the hydrodynamic performances of the two types of WEC-FB systems are studied and compared concretely. Finally, in Section 5, conclusions are drawn and recommendations are provided for applying these two types of WEC-FBs.

2 Mathematical model

2.1 Control equation

2.1.1 Flow and motion equations

The governing equations are Navier – Stokes equations based on two-dimensional unsteady, incompressible viscous fluid theory. The continuity and momentum equations are expressed as follows.

$$\nabla \cdot \boldsymbol{u} = 0 \tag{1}$$

$$\frac{\partial \boldsymbol{u}}{\partial t} + (\partial \boldsymbol{u} \cdot \nabla)\boldsymbol{u} = -\left(\frac{1}{\rho}\right)\nabla p + \left(\frac{\mu}{\rho}\right)\nabla^2 \boldsymbol{u} + F \tag{2}$$

where $\boldsymbol{u}$ is the velocity vector, μ is the dynamic viscosity coefficient, p is the pressure, ρ is the water density, and F is the mass force, and here F refers to the gravitational force.

Generally, a floating body has six degrees of freedom, but for a WEC-FB restricted by a vertical pile in this study, its primary interface is constrained to move only in heave. The heave motion equation of an integrated floating body is as follows.

$$M\frac{\partial^2 \zeta}{\partial t^2} = F_y - Mg + F_{\mathrm{PTO}} \tag{3}$$

where M is the mass of the floating body, F_y is the wave force on the floating body in the y direction, F_{PTO} is the PTO damping force reacting on the floating body, ζ is the amplitude of heave motion of the floating body, t is the time, and g is the gravitational acceleration.

The hydrodynamic force and moment are calculated by integrating the pressure on the body surface as follows:

$$\begin{cases} F_x = \iint_A \left(-p\delta_{ik}\right) n_k \mathrm{d}A \\ F_y = \iint_A \left(-p\delta_{ik}\right) n_k \mathrm{d}A \\ M_z = \iint_A \left(-p\delta_{ik}\right) n_k \cdot \boldsymbol{r}_k \mathrm{d}A \end{cases} \tag{4}$$

2.1.2 The PTO system

The PTO is considered installed to the center of mass of the floater, connected by a rigid rod, and thus the heave motion of the floater is used in the energy absorption process, as plotted in Figure 1. The PTO system can be modeled by four types, linear, speed-square, snap-through, and constant PTO damping (Huang et al., 2019). The linear PTO damping is widely employed to quantify the response of the oscillating WEC to the floater's motion for its simplicity in the governing equations. When heaves are excited by waves, the floater suffers a force from the PTO quantified as follows.

$$F_{\mathrm{PTO}} = -B_{\mathrm{PTO}}\frac{\partial \zeta}{\partial t} - K_{\mathrm{PTO}}\zeta(t) \tag{5}$$

where K_{PTO} is the spring stiffness coefficient, and B_{PTO} is the damping coefficient.

To appropriately simulate the PTO system, Madhi et al. (2014) used a fabricated permanent magnet linear generator PTO (Yeung et al., 2012) to theoretically study the energy extraction efficiency of the Berkeley wedge, where the K_{PTO} is set to zero, and only B_{PTO} is investigated. This approach makes the research simpler and more convenient. Reabroy et al. (2019) and Han et al. (2023) also used this formulation to study the PTO effect on the hydrodynamic response and power efficiency analysis of a heaving wave energy converter. Therefore, this study uses the same strategy for the PTO system as the former studies Madhi et al. (2014) concluded that an excellent energy extraction efficiency can be achieved when the floater is operating at resonance and the absorption damping B_{PTO} of the generator is matched with the radiation damping λ_{22} of the floater. λ_{22} is calculated using the potential flow code RWYADMXA based on a boundary integral equation formulation (Yeung, 1975). This code is applicable in this case because the Berkeley wedge is designed to have minimal influence from viscosity. In this study, when viscous damping is unignorable and dominant compared to potential radiation damping, as indicated in Lopez-Pavon and Souto-Iglesias (2015) and Son et al. (2016), a potential flow model such as WADAM fails to accurately capture the physics of viscous damping due to its neglect of modeling FBs with thin plates. Therefore, in this case study, a viscous model has been chosen to find the appropriate PTO damping coefficient.

2.1.3 Hydrodynamic performance parameters

η_{e}, the wave energy CWR of the integrated device, is equal to the ratio of the captured wave energy power to the incident wave power, as follows.

$$\eta_{\mathrm{e}} = \frac{E_{\mathrm{p}}}{E_{\mathrm{w}}} = \frac{\frac{B_{\mathrm{PTO}}}{nT}\int_{t}^{t+nt} v^2 \mathrm{d}t}{\frac{\rho g H_{\mathrm{i}}^2 \omega}{16} k\left(1 + \frac{2hk}{\sinh 2hk}\right)} \tag{6}$$

where E_{p} is the captured wave energy power, E_{w} is the incident wave power, B_{PTO} is the PTO damping coefficient, n is the calculated number of wave periods, t is the time, T is the wave period, v is the velocity of the buoy in heave motion, h is the water depth, k is the wave number, H_{i} is the incident wave height, and ω is the wave circular frequency.

The dissipation coefficient K_{d} of the integrated device is the ratio of the absorbed and dissipated energy by the integrated device to the incident wave energy, including the energy captured by the WEC, the kinetic energy generated by the movement of the floater, and the energy dissipated by the vortex. K_{d} satisfies the following formula.

$$K_{\mathrm{d}} = 1 - C_{\mathrm{t}}^2 - C_{\mathrm{r}}^2 \tag{7}$$

where C_{t} is the transmission coefficient, and C_{r} is the reflection coefficient.

2.2 Numerical solution

2.2.1 Flow equation solution

The momentum equation of Eq. (2) is solved using a fractional step method in the orthogonal Cartesian coordinate system. The convection flow as Eq. (8) is solved discretely using a constrained interpolation profile method (Yabe et al., 2001; Hu and Kashiwagi, 2004) with third-order accuracy, which is a compact high-order scheme using two grid points information to reduce numerical diffusion.

$$\frac{\partial \boldsymbol{u}_i}{\partial t} + \boldsymbol{u}_j\frac{\partial \boldsymbol{u}_i}{\partial x_j} = 0 \tag{8}$$

The diffusive flow is solved using the central difference method. The pressure term is solved using the SOR successive overrelaxation method. Through this method, Zhao and Hu (2012) established a numerical model for simulating the violent interaction of a freak wave and a floating body and verified that this model has good spatial–temporal convergence and numerical stability.

2.2.2 Boundary solutions

The water–air flow with a solid structure is treated as a multiphase flow problem that includes water, air, and a solid

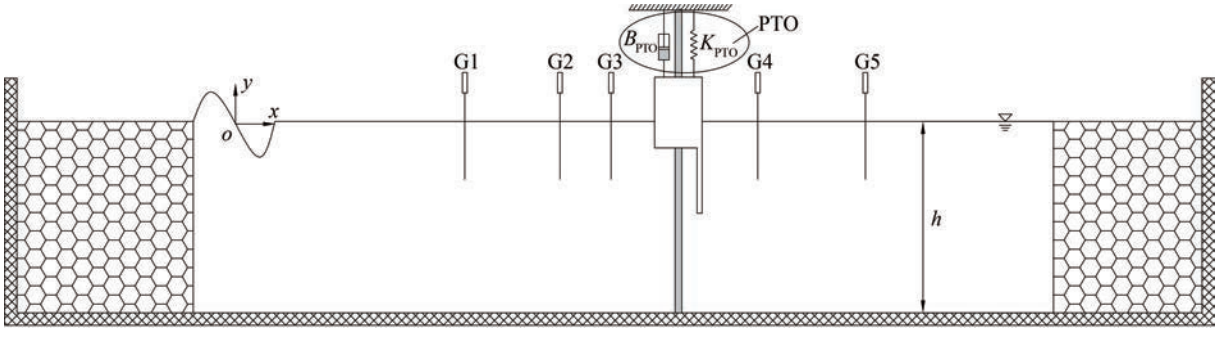

Figure 1 Computational domain with the presence of the WEC-FB

body in a Cartesian coordinate system. The VOF method is used to handle the interface of multiphases in the grid. The volume function is introduced and determined using the convection equation:

$$\frac{\partial \varphi_n}{\partial t} + \boldsymbol{u}\nabla\varphi_n = 0 \tag{9}$$

where φ_n (n = 1, 2, 3) is the volume function of water, air, and solid, respectively, satisfying $0 \leqslant \varphi_n \leqslant 1$ and $\varphi_1 + \varphi_2 + \varphi_3 = 1$. After obtaining φ_n, the physical property γ in a cell grid, such as the density or the viscosity, can be calculated by averaging as following:

$$\gamma = \varphi_1\gamma_1 + \varphi_2\gamma_2 + \varphi_3\gamma_3 \tag{10}$$

To capture the violent free surface, a tangent of hyperbola scheme with slope weighting named THINC/SW (Xiao et al., 2005) is used. The virtual particle method is used to accurately construct and reconstruct the geometry of the solid.

To couple the interface of fluid and solid interaction between floater and fluid, the immersed boundary method is used. The interaction of the floater and the flow is considered by imposing the floater velocity into the flow at the solid boundary. More details can be found in Hu and Kashiwagi (2004). To update the local velocity of the fluid domain containing the solid, the following equation is introduced.

$$\boldsymbol{U} = \boldsymbol{U}_{\mathrm{b}}\phi_3 + \boldsymbol{u}(1 - \phi_3) \tag{11}$$

where $\boldsymbol{U}$ is the coupled velocity of the fluid containing the solid body, $\boldsymbol{U}_{\mathrm{b}}$ is the local velocity of the body, $\boldsymbol{u}$ is the velocity obtained using Eq. (2), and ϕ_3 is the volume of the solid phase.

In this model, a source wave-maker is used to generate incident waves. Two sponge layers are arranged at the two ends of the flume to absorb the passing waves. Therefore, the reflected waves from the structure can pass through the wave-maker region without disturbing the wave generation and are finally absorbed by the sponge layers. The momentum source function is derived by Choi and Yoon (2009) and Li et al. (2018):

$$s = -g(2\beta x)\exp(-\beta x^2)(D/\omega)\sin(-\omega t) \tag{12}$$

where ω is the wave angular frequency, β is the parameter associated with the width of the source function, and D is the source function amplitude, which is determined from the target wave characteristics.

2.2.3 Motion equation solution

The motion equation of the floating body in Eq. (4) is solved using the fourth-order Runge–Kutta method, which was used by Zhu (2006) to analyze the problem of ship motions.

$$\begin{cases} \zeta_{n+1} = \zeta_n + \mathrm{d}t \cdot \left(\dfrac{\partial\zeta}{\partial t}\right)_n + \mathrm{d}t \cdot \dfrac{k_1 + k_2 + k_3}{6} + o(\mathrm{d}t^5) \\ \left(\dfrac{\partial\zeta}{\partial t}\right)_{n+1} = \left(\dfrac{\partial\zeta}{\partial t}\right)_n + \dfrac{k_1}{6} + \dfrac{k_2}{3} + \dfrac{k_3}{3} + \dfrac{k_4}{6} + o(\mathrm{d}t^5) \\ k_1 = \mathrm{d}t \cdot f\left[t, \zeta_n, \left(\dfrac{\partial\zeta}{\partial t}\right)_n\right] \\ k_2 = \mathrm{d}t \cdot f\left[t + \dfrac{\mathrm{d}t}{2}, \zeta_n + \dfrac{\mathrm{d}t \cdot \left(\dfrac{\partial\zeta}{\partial t}\right)_n}{2}, \left(\dfrac{\partial\zeta}{\partial t}\right)_n + \dfrac{k_1}{2}\right] \\ k_3 = \mathrm{d}t \cdot f\left[t + \dfrac{\mathrm{d}t}{2}, \zeta_n + \dfrac{\mathrm{d}t \cdot \left(\dfrac{\partial\zeta}{\partial t}\right)_n}{2} + \dfrac{\mathrm{d}t \cdot k_1}{2}, \left(\dfrac{\partial\zeta}{\partial t}\right)_n + \dfrac{k_2}{2}\right] \\ k_4 = \mathrm{d}t \cdot f\left[t + \mathrm{d}t, \zeta_n + \mathrm{d}t \cdot \left(\dfrac{\partial\zeta}{\partial t}\right)_n + \dfrac{\mathrm{d}t \cdot k_2}{2}, \left(\dfrac{\partial\zeta}{\partial t}\right)_n + k_3\right] \end{cases} \tag{13}$$

where ζ_n is the floater position at timestep n, ζ_{n+1} is the floater position at timestep $n + 1$, $\left(\dfrac{\partial\zeta}{\partial t}\right)_n$ is the v velocity at timestep n, $f\left[t, \zeta_n, \left(\dfrac{\partial\zeta}{\partial t}\right)_n\right]$ is the equation of motion function determined by Eq. (3), dt is the time step, and $o(\mathrm{d}t^5)$ is the error.

3 Numerical model settings and Validation

3.1 Numerical wave tank

The target application sea is nearshore water, with the assumption that the water depth is 30 – 50 m, the wave height is 2.0–3.0 m, and the wave period is 5.0–9.0 s. A scale of 1:20 is used in the numerical calculation. Therefore, a 2D numerical wave tank is set as 32 m long and 1.5 m deep, as shown in Figure 1. Two wave-absorbing regions are 8 m long and set at each end of the flume to reduce the wave reflection. The model of the integrated WEC-FB is placed at x = 5.5 – 5.73 m in the flume, and five wave height measuring points are arranged in the front and back sides of the model, as shown in Table 1.

Table 1 Positions of five wave gauges in the wave tank used in the present analysis

Gauge number	G1	G2	G3	G4	G5
Position in x (m)	3.0	3.25	5.4	9.00	9.25

3.2 WEC-FB model settings

The parameters of the integrated WEC-FB are designed

based on the experiment of Madhi et al. (2014). Therefore, the scaled model parameters are as follows: box width B = 0.23 m, box draft D = 0.15 m, and wave baffle or triangle height d = 0.55 m, see Figure 2. In these parameter settings, the total draft of the WEC-FB ($D + d$) for the trapezoidal type and L type remains unchanged, set as $D + d$ = 0.70 m. Thus, their displacement and mass are different. The total mass of the trapezoidal type floater is M_1 = 97.75 kg, and that of the L type floater is M_2 = 56.50 kg. To investigate the influence of the displacement and box draft on the hydrodynamic characteristics of the integrated WEC-FB, another set of parameters is designed under the principle of the same displacement (V_1) or box draft (D_0) for comparison, see Figure 3. In addition, a set of dimensions of the L type with the same natural frequency as the trapezoidal type (D_2, V_2) and a smaller draft of the L type (D_3, V_3) are examined for comparison, see Table 2.

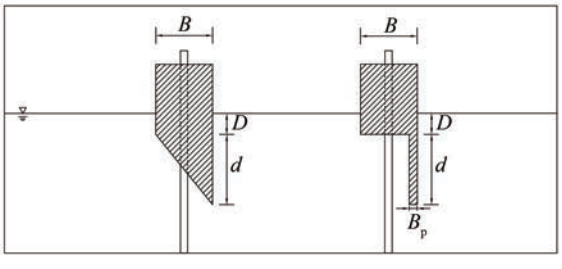

Figure 2 Parameter definition of trapezoidal type and L type WEC-FBs

A suitable dimension parameter for the buoy can bring the natural frequency of the buoy closer to the incident wave frequency to create the resonance in the buoy motion. In potential theory, the heave natural frequency of the buoy can be obtained as follows:

$$\omega_n = \sqrt{\frac{B_{\mathrm{PTO}} + K_{\mathrm{hys}}}{m + a_z}} \tag{14}$$

where a_z is the added mass coefficient, and K_{hys} is the hydrodynamic restoring coefficient. For a disc oscillating perpendicularly to its plane, the theoretical coefficient of added mass based on Sarpkaya and Isaacson (1982) is $a_z = \frac{1}{3}\rho D_{\mathrm{d}}^3$. For a hemispherical buoy with diameter D, the theoretical coefficient of added mass based on Korotkin (2009) is $a_z = \frac{1}{24}\rho\pi D^3$. However, for the other irregular shapes, an analysis of a semi-submersible Floating Offshore Wind Turbine (FOWT) with a heave plate by Lopez-Pavon and Souto-Iglesias (2015) noted that added mass coefficient values predicted with the potential solver (WADAM) are insufficiently accurate because it neglects modeling thin plates with doublets.

To analyze the natural period of the WEC-FB, calculations of the free decay test were performed. Figure 4 shows the results for the three cases in Table 2. A dimensionless parameter of the natural period, defined as $T_n{*} = T_n(B/g)^{0.5}$, was also calculated. It is seen that the natural period of the trapezoidal-type floater is T_n = 1.45 s. For the L type floater, the natural period is approximately T_n = 1.32 s in the case of V_0 and approximately T_n = 1.54 s, 1.45 s, and 1.25 s in the cases of V_1, V_2, and V_3, respectively, as listed in Table 2, indicating that the natural period of the floater increases with the displacement volume.

3.3 Wave conditions

In this study, the influence of the wave period, PTO damping, and buoy draft on hydrodynamic and energy capture performances is investigated under regular wave conditions. Because the operation wave conditions in the target application sea are H = 1.0–3.0 m and T = 5.0–9.0 s, the wave conditions for operation mode are chosen as H = 0.05–0.1 m and T = 1.1–2.0 s on a scale of 1∶20 in the numerical model. To study the influence of PTO damping on the hydrodynamic characteristics, five PTO damping coefficients are analyzed in each wave condition, as shown in Table 3.

3.4 Model validation

3.4.1 Verification of regular wave generation

Before calculating the interaction of waves with the WEC-FB, we simulated the wave generation and propagation of the regular wave in the numerical wave tank without the WEC-FB to verify its wave generation capability and wave propagation stability. The target wave has A = 0.062 5 m and T = 1.58 s. Figure 5 shows a comparison between the numerical wave generation results and the theoretical solutions. For the regular wave, the amplitude and period of the numerical wave agree well with those of the theoretical wave, with a relative error of 5%. Thus, the wave generation accuracy meets the requirements.

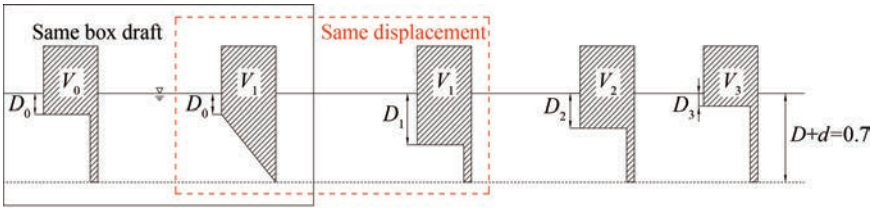

Figure 3 Settings for the influence of the displacement and box draft of the WEC-FB

Table 2 Parameters for the influence of displacement and box draft

Structure type	Box draft D (m)	Displacement V (m^3)	Natural period T_n (s)	Natural period T_n*
L type	0.15 (D_0)	0.056 5 (V_0)	1.32	0.20
Trapezoidal type	0.15 (D_0)	0.097 8 (V_1)	1.45	0.22
L type	0.1 (D_3)	0.047 0 (V_3)	1.25	0.19
L type	0.25 (D_2)	0.075 5 (V_2)	1.45	0.22
L type	0.36 (D_1)	0.097 8 (V_1)	1.54	0.24

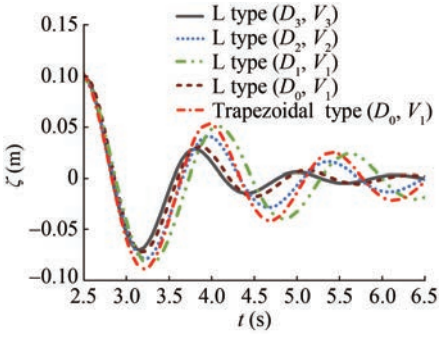

Figure 4 Free damping test

Table 3 Wave conditions for operation mode

Wave height H (m)	Wave period T (s)	$T^* = T\sqrt{B/g}$	Wavelength L (m)	PTO damping coefficient B_{PTO} (kg/s)
0.05	1.1	0.17	1.90	60, 100, 150, 200, 250
0.1	1.2	0.18	2.29	60, 100, 150, 200, 250
	1.4	0.21	3.08	60, 100, 150, 200, 250
	1.58	0.24	3.87	100, 150, 200, 250, 300
	1.79	0.27	4.83	100, 150, 200, 250, 300
	2.0	0.31	5.80	100, 150, 200, 250, 300

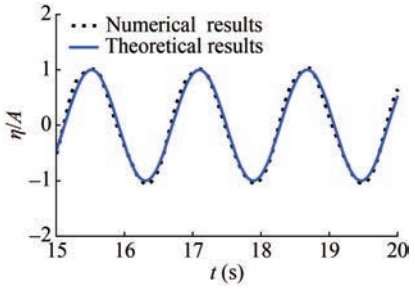

Figure 5 Comparison of numerical wave generation and the theoretical wave

3.4.2 Grid convergence study

The simulations of a periodic wave interacting with the heave motion of the WEC-FB in seven grids (Grid 1–Grid 5 listed in Table 4) are performed to verify the stability and accuracy of the model. The grids are nonuniform in the computational domain and are fined around the structure and the free surface, which is shown in Figure 6. The comparison results of the velocity and amplitude of heave motion response and vertical wave force on the floater are shown in Figure 7. Figure 7(a) shows comparisons of the calculation results for different grids. We found that coarse meshes agree well with fine meshes, except for a slight difference in the peaks and troughs. Figure 7(b) shows the peak values and residual errors of four other grids compared to those of the finest grid. It is seen that the residual errors of Grid 1 and Grid 2 are within a range of 7%, slightly larger than those of the other grids at some time instances. The results of Grid 3 and Grid 4 are almost identical, with residual errors of less than 5%. Therefore, the grid convergence of the model is satisfied. For the sake of computational efficiency and better capture of the wave–structure interaction process, the finer mesh resolutions of 0.4 cm in the x direction and 0.1 cm in the y direction are adopted in the following computations.

Table 4 Grid settings for grid convergence study

Grid	Mesh number	Min Δx (cm)	Min Δy (cm)
Grid 1	602×330	0.8	0.5
Grid 2	602×680	0.8	0.2
Grid 3	718×680	0.4	0.2
Grid 4	718×1 260	0.4	0.1
Grid 5	958×1 260	0.2	0.1

3.4.3 Verification of the wave–structure interaction

The experiment performed by Koutandos et al. (2005) is used to verify the accuracy of the wave–structure interaction by the numerical model. A square box model with a height of 0.09 m, a width of 0.3 m, and a draft of 0.067 5 m was set up in a wave flume with a water depth of 0.4 m. C_t is compared with the experimental results of Koutandos et al. (2005) in Figure 8, along with numerical results by Liu (2008). These comparisons show that the results of C_t simulated by this model are basically consistent with the experimental results of Koutandos et al. (2005) and show better agreement than the numerical results of Liu et al. (2008). The maximum error is approximately 7%. Therefore, the accuracy of simulation results for wave–structure interaction in this study can be considered acceptable.

4 Hydrodynamic and energy capture performance

4.1 Effect of the PTO damping coefficient

PTO coefficients provide a critical role in the energy cap-

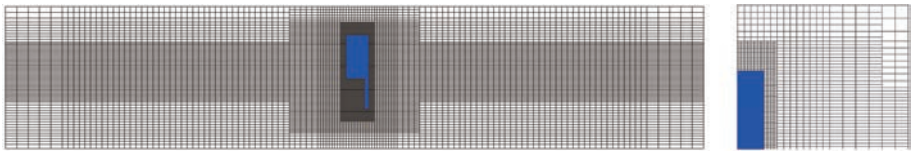

Figure 6 Grid generation details of the wave tank model

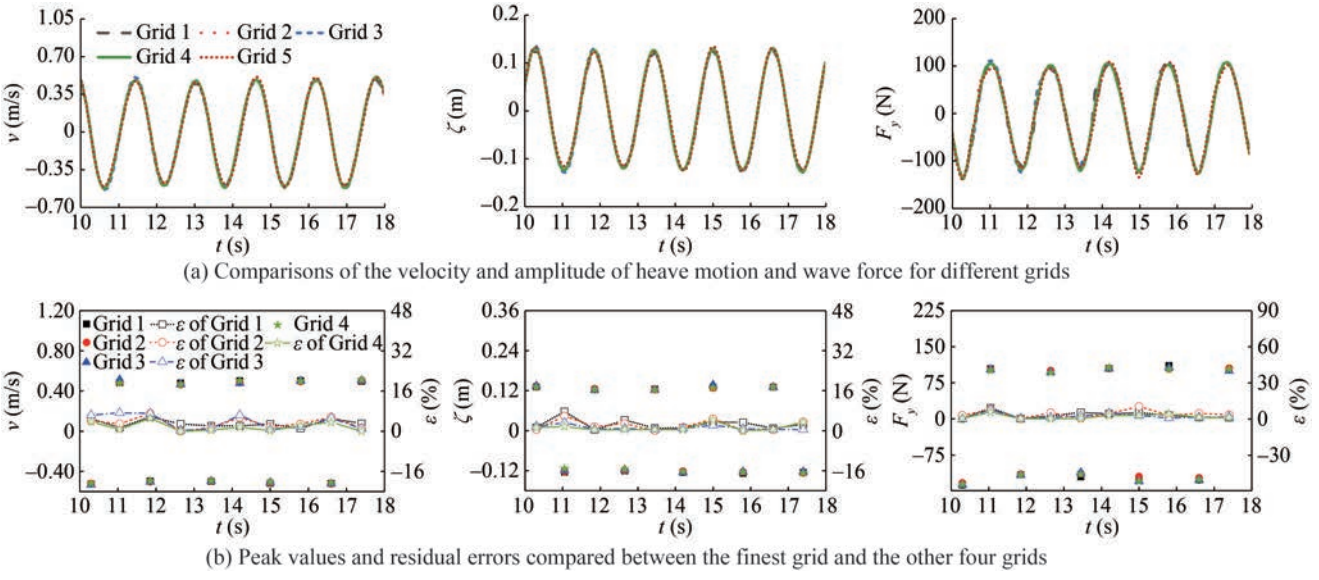

Figure 7 Grid convergence results for the velocity and amplitude of heave motion and wave force

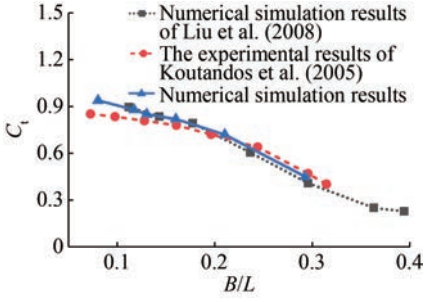

Figure 8 Comparison of wave attenuation performance

ture performance of the heaving buoy WEC. Tuning the WEC to resonate by adjusting the spring and damper characteristics of the PTO can maximize the wave energy capture efficiency. According to the research conclusion of Ning et al. (2016), there exists an optimal PTO damping coefficient B_{oPTO} in a wave period for achieving the highest energy capture performance. This section performed 30 computations with PTO damping coefficient B_{PTO} = 60, 100, 150, 200, 250, and 300 kg/s under wave period T^* = 0.17, 0.18, 0.21, 0.24, 0.27, and 0.31, defined as $T^* = T(B/g)^{0.5}$, to estimate the trend of CWR with the variation in the PTO damping coefficient.

Figure 9 shows the variations in CWR (η_e) in each wave period for the two floater types. The figures show that there is a common trend in the variation in the CWR (η_e), i.e., the CWR (η_e) first increases and then decreases with the variation in B_{PTO} in each wave period, meaning that there exists an optimal B_{oPTO}. However, the optimal B_{oPTO} of the two types of WEC-FBs differs among wave periods.

Surprisingly, in shorter wave periods T^*<0.21, the CWR (η_e) of the L type (D_0, V_0) in each B_{PTO} is higher than that

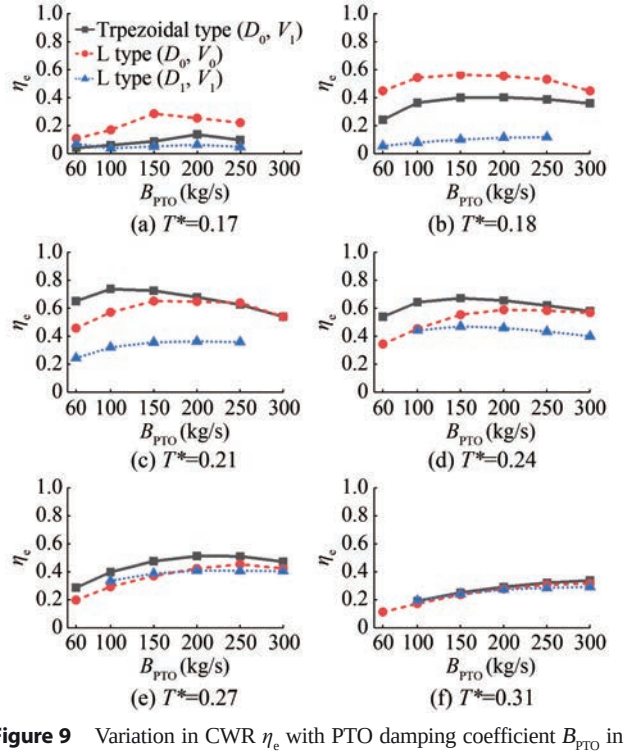

Figure 9 Variation in CWR η_e with PTO damping coefficient B_{PTO} in each wave period

of the trapezoidal type with the same box draft D_0, which is inverse to the hypothesis that the CWR (η_e) of the L type might be lower than that of the trapezoidal type. This indicates that the damper characteristics of the PTO cannot be adjusted, even for the trapezoidal type. In terms of engineering application, because the L type dimensions (D_0, V_0) have a smaller displacement volume than the trapezoidal-type dimensions (D_0, V_1), its instruction cost would be less. Hence, in terms of performance and economy in shorter waves, the L type is more competitive than the trapezoidal type in the same box draft condition.

In contrast, in intermediate wave periods $T^* = 0.21–0.24$, the CWR (η_e) of the trapezoidal type is considerably larger than that of the other two L-type dimensions. In longer wave periods $T^* = 0.27–0.31$, the difference in CWR (η_e) among different dimensions is negligible, and all the values of η_e are less than 35%. One explanation for this discrepancy is that the three dimensions have different natural periods, i.e., $T_n^* = 0.22$ for the trapezoidal type (D_0, V_1) and $T_n^* = 0.20$ for the L type (D_0, V_0). Thus, when the wave period is close to the natural period, the resonance can occur and consequently produce the largest heave motion, resulting in the highest CWR (η_e). Figure 10 plots the heave velocity against B_{PTO} in each wave period. In wave period $T^* = 0.18$, the heave velocity is higher for the L type (D_0, V_0) than for the other two dimensions, verifying the conjecture that the buoy resonates with the incident wave.

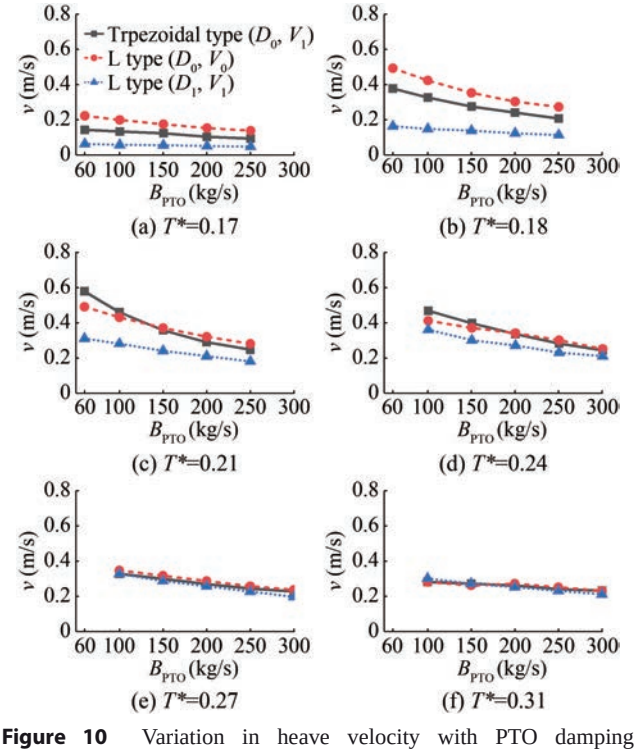

Figure 10 Variation in heave velocity with PTO damping coefficient B_{PTO} in each wave period

Figure 11 and Table 5 show the optimal B_{oPTO} for the three structure dimensions in each wave period. These figures and data show that the optimal B_{oPTO} differs among waves and structure dimensions. B_{oPTO} first decreases and then increases with increasing wave period. The increasing trend with the wave period is due to waves with longer periods carrying more energy and thus inducing more intense heave motion, resulting a larger PTO damping force. Comparing the B_{oPTO} shows that the trapezoidal type has the smallest B_{oPTO} among the three dimensions in each wave period, meaning that its radiation damping is the lowest, which will be further demonstrated in Section 4.4.

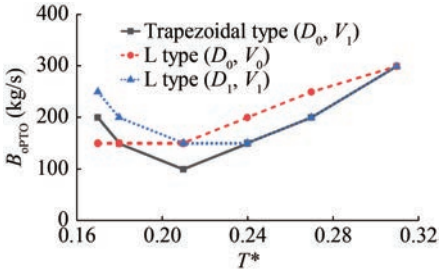

Figure 11 Variation in the optimal PTO damping coefficient B_{oPTO} with wave period

Table 5 Optimal PTO damping coefficient B_{oPTO} in each wave period for the three structure types

	Structure type	Wave period T^*					
		0.17	0.18	0.21	0.24	0.27	0.31
Optimal PTO damping coefficient B_{oPTO} (kg/s)	Trapezoidal type (D_0, V_1)	200	150	100	150	250	300
	L type (D_0, V_0)	150	150	150	200	250	300
	L type (D_1, V_1)	250	200	150	150	200	300

Notably, at the natural period for the three dimensions, B_{oPTO} becomes the smallest among the wave periods studied for all structure dimensions. This result is consistent with the resonance of the buoy and the incident wave, as a large amount of movement is contributed by a small amount of PTO damping force.

Figure 12 shows the variations in C_t in each wave period for the two floater types. As seen in the figures, C_t is barely influenced by the PTO damping coefficient B_{PTO}. In shorter waves ($T^* < 0.21$), the three structure dimensions differ quite negligible, while in longer waves ($T^* > 0.24$), there exist a substantial gap between the structures representing by two box drafts of D_0 and D_1. This gap indicate that the box draft has a greater effect on C_t than the structure type.

In more detail, the variation trend of C_t with the PTO damping coefficient transforms from an increase to a decrease at $T^* = 0.18$, 0.24, and 0.21 for the case (D_0, V_0) of L type, the case (D_1, V_1) of L type, and for the trapezoidal type, respectively. That is, C_t increases very slightly with increasing PTO damping coefficient at shorter waves, but the trend becomes decreasing at longer waves. This may correlate to the natural period of the floaters, $T_n^* = 0.20$ and 0.24 for the case (D_0, V_0) and (D_1, V_1) of L type respec-

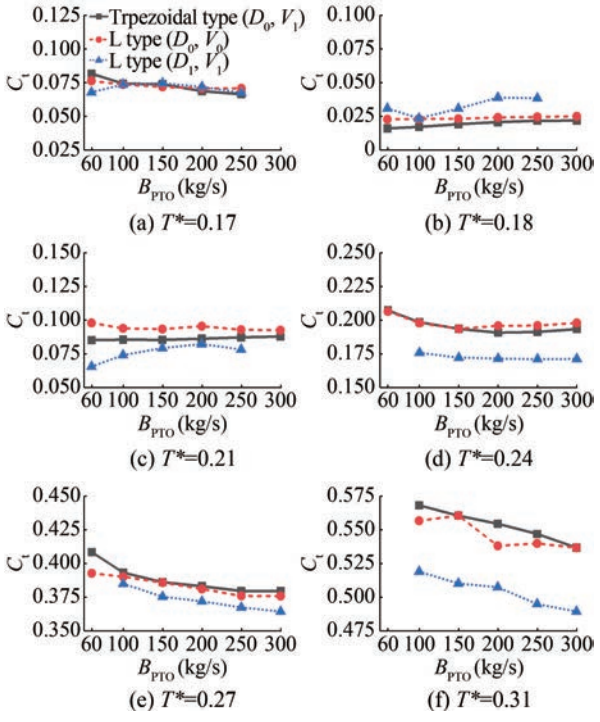

Figure 12 Variation in transmission coefficient C_t with PTO damping coefficient B_{PTO} in each wave period

tively, and T_n* = 0.22 for the trapezoidal type. In shorter waves, a smaller PTO damping coefficient might promote the resonance of the waves and the floater, resulting in a larger heave motion that generates radiation waves. These radiation waves may disturb the transmitted waves and result in a smaller transmission coefficient.

4.2 Effect of wave period

To study the influence of the wave period T on the hydrodynamic and energy capture performances of the two structure types, C_r, C_t, K_d, and CWR (η_e) at the optimal PTO damping coefficient are plotted versus the dimensionless wave period T* in Figure 13.

In Figure 13(a), the wave reflection coefficients for the two structure types first decrease substantially and then increase with increasing wave period, and the reflection coefficient reaches the minimum at T* = 0.21. In Figure 13(b), the two structure types have almost the same transmission coefficient curves, indicating that their wave protection performances are not considerably different. The variation curves show the same increasing trend with increasing wave period, and all the values are smaller than 0.5, with the exception of C_t = 0.536 at T* = 0.24. Koutandos et al. (2005) and He et al. (2013) noted that the C_t of a breakwater should satisfy C_t < 0.5 in its normal operation conditions. Therefore, it can be concluded that both structures have satisfactory wave protection performances. Figures 13(c)–13(d) shows that K_d and CWR (η_e) of the two structural types first increase and then decrease with increasing wave period, and both types reach the maximum at T* = 0.21. This phenomenon arises because the natural period of the WEC-FB for both structure types is near this wave period, close to the resonance condition. Consequently, the incident wave energy is transformed and absorbed in terms of heave motion and energy conversion by the integrated device, reducing the reflection coefficient, consistent with the conclusion of Zhang et al. (2020).

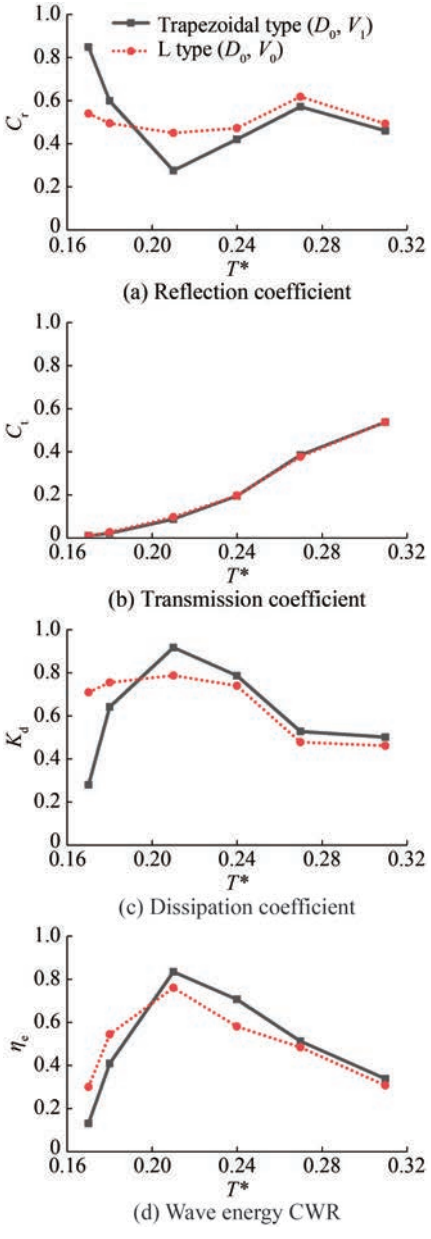

Figure 13 Comparisons of hydrodynamic performances with the variation in wave periods for the two types

More evidence for the resonance is found in Figure 14 and Figure 15. Figure 14 compares the time history of heave motions for both structures at each wave period. The heave motion of the L type is larger than the trapezoidal type at T* = 0.17–0.18 and vice versa at T* = 0.21. Figure 15

demonstrates the heave motions with the variation in wave period, which coincides with the resonance phenomena. For the trapezoidal type, the highest amplitude of heave motion in all the wave periods is at T^* = 0.21, coinciding with its natural period T_n^* = 0.22; for the L type, near T^* = 0.18, almost equal to its natural period T_n^* = 0.20.

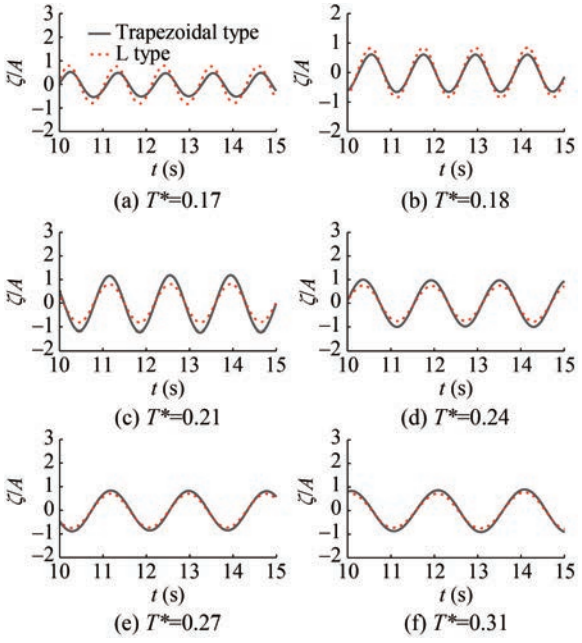

Figure 14 Time history of heave motions for the two types in different wave periods

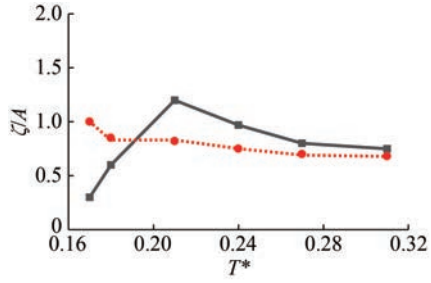

Figure 15 Heave motions with the variation in wave periods for the two types

Comparing the energy capture performances of the two types in Figures 13(c)−13(d) shows that for shorter wave period T^*<0.21, the K_d and CWR (η_e = 54.4%) of the L type are better than those of the trapezoidal type (η_e = 40.8%). In the intermediate wave period T^* = 0.21−0.24, the trapezoidal type with a maximum of η_e = 83.5% outperforms the L type with a maximum of η_e = 76.1%. For the longer wave period T^*>0.27, their performances are much the same. C_r in Figure 13(a) shows the similar performances of the two types. It reveals that the L type can absorb wave energy in a shorter wave period range than the trapezoidal type with the same draft settings. In engineering applications, manufacturing and installing this type of floater is easier and less expensive because of the separated right-angle geometry and a smaller displacement volume.

To interpret the physical mechanism of the phenomenon, the force responses of the two types are analyzed in Figures 16(a)–16(b). Apparently, the variation in F_x is opposite to that of the F_y. For the trapezoidal type, F_x decreases and then increases with increasing wave period, whereas F_y increases and then decreases. For the L type, F_x increases as the wave period increases, while F_y decreases. For the two types, F_x reaches the minimum at their resonant period respectively, and F_y reaches the maximum. By comparing to the variation in CWR, we can infer that minimizing force F_x while enhancing force F_y will increase the CWR.

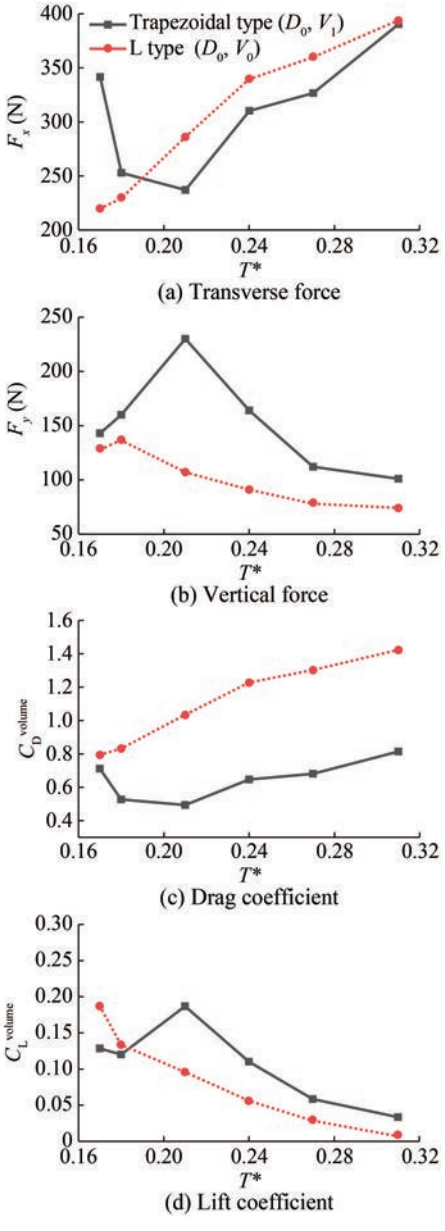

Figure 16 Force responses and coefficients with the variation in wave periods for the two types

Next, the drag and lift coefficients influenced by the displacement volume are defined as follows.

$$C_{\mathrm{D}}^{\mathrm{volume}} = \frac{F_x}{\frac{1}{2}\rho g V} \tag{15}$$

$$C_{\mathrm{L}}^{\mathrm{volume}} = \frac{F_y - F_{\mathrm{PTO}}}{\rho g V} \tag{16}$$

where D is the box draft, and V is the displacement volume.

In Figures 16(c)–16(d), the drag and lift coefficients are plotted against the wave period. The variation trend of the drag coefficient is opposite to that of the lift coefficient, similar to the force responses. Notably, the lowest drag coefficient is found near the resonant period of $T^* = 0.21$ for the trapezoidal type and $T^* = 0.18$ for the L type. At the same time, the highest lift coefficient is found near the resonant period, corresponding to the highest range of the energy capture performance. In addition, at $T^* = 0.17 – 0.18$, the lift coefficient for the L type is higher than that of the trapezoidal type and vice versa at $T^* = 0.21–0.31$. This comparison indicates that the lift coefficient C_{L} could be used to evaluate and compare energy capture performances.

Therefore, in terms of energy capture efficiency, when the floater resonates with the incident wave, the best hydrodynamic performance is reached for both types. Because they resonate at different frequencies, they are designed to work best in a specific wave condition. At shorter wave periods of $T^* = 0.17–0.18$, the L type has more competitiveness with a higher CWR and less cost. At intermediate wave periods of $T^* = 0.21–0.24$, the trapezoidal type has a higher CWR but more cost because of the larger displacement volume. At relatively longer wave periods, because no resonance occurs to any structure type, their performances are considerably more similar.

4.3 Effect of box draft and displacement

For a rectangular WEC-FB, assuming a constant width, variation in floater draft is inevitable in designing a new geometry. A suitable draft for the floater can make the natural frequency of the floater become closer to the incident wave frequency to create the resonance in the floater motion. For an irregular bottom geometry, the draft is insufficient to represent the added mass, so the volume of the base geometry or the displacement volume should be checked.

The main assumption in the design of the WEC-FB is that the maximum power should be captured from the incident wave and the transmitted wave should be minimal, although these aims would be difficult to reach simultaneously. In addition, the costs regarding installation, transportation, and manufacturing are major parameters for comparing different floater geometry designs.

In the above sections, the cases we discussed have the same box draft and different displacement volumes, referring to the settings of (D_0, V_0) for the L type and (D_0, V_0) for the trapezoidal type, as listed in Table 2. In these cases, the displacement volume of the L type ($V_0 = 0.056\ 5\ \mathrm{m}^3$) is smaller than that of the trapezoidal type ($V_1 = 0.097\ 8\ \mathrm{m}^3$). Some researchers set the basic dimension to have the same mass and displacement to investigate the hydrodynamic performance for different shapes of WEC (Reabroy et al. 2019). Therefore, this section discussed and compared two basic dimensions, one with the same box draft (D_0) and a different displacement volume (V_0, V_1), the other with the same displacement volume (V_1) and a different box draft (D_0, D_1). In the dimension with the same displacement volume (V_1), the box draft of the L type ($D_1 = 0.36$) is larger than that of the trapezoidal type ($D_0 = 0.15$). Moreover, to interpret the influence of draft and displacement volume, a set of dimensions of the L type with the same natural frequency as the trapezoidal type (D_2, V_2) and a smaller draft of the L type (D_3, V_3) is examined for comparison, as listed in Table 2.

Figure 17 shows the hydrodynamic performance of the two structure types in different wave periods in terms of C_{r}, C_{t}, K_{d}, CWR (η_{e}), difference value $\Delta = C_{\mathrm{d}} - \eta_{\mathrm{e}}$, and heave motion ζ/A. The PTO is set as the optimal PTO damping coefficient corresponding to each wave period. For a better view of the effect of the box draft or displacement volume, Figure 18 illustrates the hydrodynamic performance of the L type plotted against the box draft/displacement volume in each wave period

Figures 17(a)–17(d) shows that there exists one trough of C_{r} and one peak of η_{e} in the range of $0.18<T^*<0.24$ for different structure dimensions, indicating that the wave reflection capability of these structures is poor in this range. This finding agrees with the resonant phenomenon of the incident wave with a specific structure dimension, see Section 4.2.

As shown in Figure 18, with an increase in the box draft from D_3 to D_1 for the L type, C_{r} increases and C_{t} decreases, indicating that the wave protection performance of the L type is improved, and the improvement of C_{t} is obvious when the wave period is small. By comparing the two types with the same box draft D_0, the cases of (D_0, V_0) for the L type and (D_0, V_1) for the trapezoidal type in Figure 17(b), it is found C_{t} is not considerably influenced by displacement volume and structure type. Moreover, by comparing the two types with the same displacement volume V_1, the cases of (D_1, V_1) for the L type and (D_0, V_1) for the trapezoidal type, it is found that as the box draft increases from D_0 to D_1, more wave energy is reflected and less energy is transmitted, meaning that the box draft has a substantial effect on the wave protection performance. This effect is consistent with the diffraction characteristic of surface waves with their energy concentrated on the water surface, where a wave with a longer period will diffract over a longer distance. When the box draft increases, it actually increases the draft at the front of the floater, which will directly interfere with the diffraction of the shorter wave and reduce reflection. In contrast, the longer period waves will be disturbed

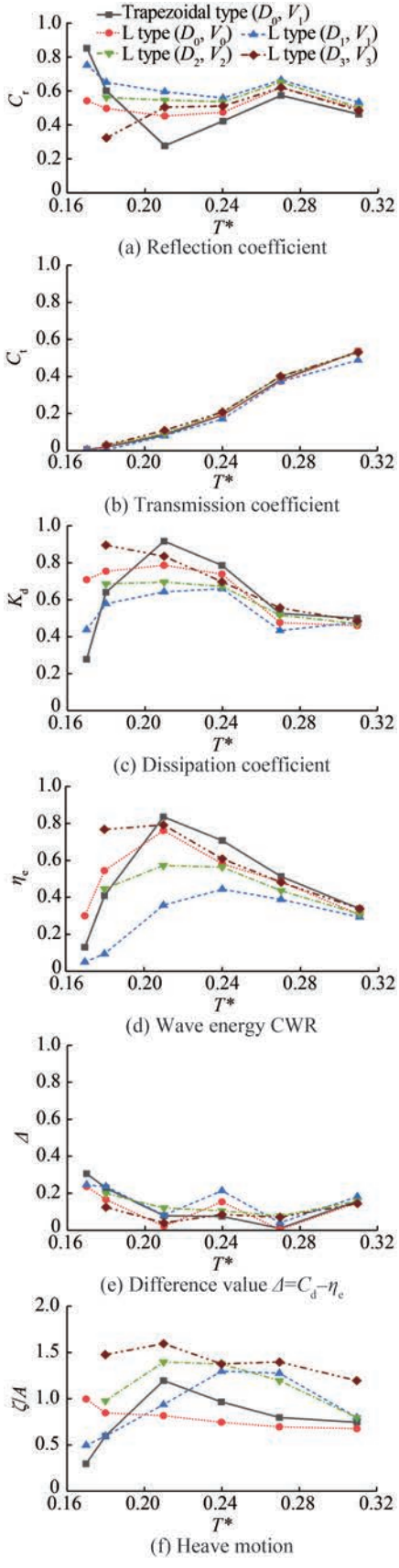

Figure 17 Comparisons of hydrodynamic performances for the two types with different box drafts and displacements

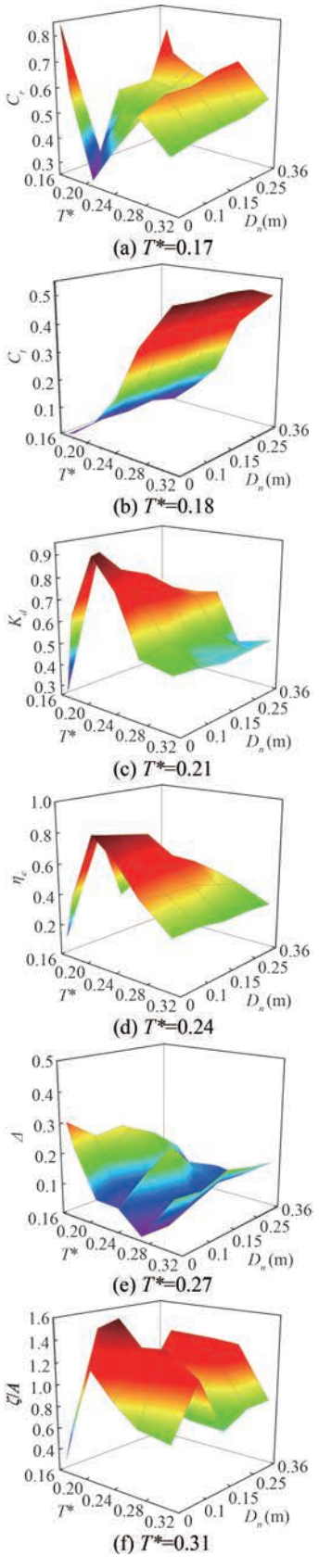

Figure 18 Comparison of hydrodynamic performance versus wave period T and box draft *D*

into high-frequency waves, thus preventing the waves from being transmitted over a longer distance. This coincides with the comparison in terms of wave reflection by Ji et al. (2021) of wave baffle attached to the front or rear side of the box. Thus, from the perspective of wave protection, the L type with a deeper box draft has the best performance among these cases.

Figure 18 shows that the value of the CWR decreases with increasing box draft for the L type. This result is reasonable, because more wave is reflected as the box draft increases and less energy is captured since wave power is mostly concentrated on the water surface. In Figures 17(c)–17(d), the dimension of the trapezoidal type has the highest CWR value, with η_e = 83%, and the L type with the smallest box draft and displacement volume (D_3, V_3) has the second highest, with η_e = 79%. This comparison implies that the trapezoidal type still has a better energy capture performance than the L type in terms of maximum CWR. However, the two dimensions differ by no more than 5%. In addition, over a shorter period T^* = 0.17–0.18, the L type has a higher CWR, exceeding 37% for the case of (D_3, V_3) and 14% for the case of (D_0, V_0). Therefore, if the predominant wave period of the operation sea area is shorter, the L type has a good potential in wave energy capture.

For a given displacement volume, the CWR of the L type (D_1, V_1) is smaller than that of the trapezoidal type (D_0, V_1) in all the wave ranges, differing by 39% at the peak of η_e. This inequality is due to the increased draft of the box, which causes more energy to be reflected as C_t in Figure 17(a) and more energy to be converted to the kinetic energy of the floater as ζ in Figure 17(d). Thus, the L type with larger displacement volume has the worst performance among the five cases in terms of energy capture performance. In engineering applications, if we only consider the displacement volume as the material cost, the trapezoidal type is a better choice with a higher CWR.

Figure 17(a), (c), (d) shows that the five dimensions achieve their best performance in terms of reflection, dissipation, and energy capture at their respective natural period. As discussed in Section 4.2, these are induced by the resonance between the waves and the floaters. The heave motions in Figure 17(f) demonstrate the resonance phenomena and reach their maximum at the corresponding wave period. More specifically, Table 6 shows the corresponding wave period of the highest heave motion and CWR for different structure dimensions, and it is seen that the heave motion and CWR peak near $T^* = T_n^*$. By adjusting the natural period of the floater with the box draft, displacement, and geometry, the WEC-FB will capture wave energy efficiently in different incident wave conditions.

In Section 4.2, to interpret the physical mechanism of the phenomenon, the drag and lift coefficients influenced by the displacement volume are introduced and analyzed. Here, to consider the effect of the draft of the box, the drag and lift coefficients influenced by the draft are given as follows.

$$C_{\mathrm{L}}^{\mathrm{draft}} = \frac{F_y - F_{\mathrm{PTO}}}{\frac{1}{2}\rho D B_z C_{\mathrm{w}}^2} \tag{17}$$

$$C_{\mathrm{D}}^{\mathrm{draft}} = \frac{F_x}{\frac{1}{2}\rho D B_z C_{\mathrm{w}}^2} \tag{18}$$

where D is the draft of the box, B_z is the width of the floater in the z direction, and C_w is the wave phase velocity, $C_w = \frac{L_w}{T_w}$.

In Figure 19, the drag and lift coefficients influenced by the draft and displacement volume are plotted against the wave period. For the L type with different drafts or displacements, C_D^{draft} and C_L^{draft} decrease as the box draft increases. Hence, the (D_3, V_3) with a minimum box draft in the L geometry type results in the highest drag and lift coefficient, which may be effective for wave energy capture based on the same other parameters, thus providing a design for parameter optimization in one geometry type.

The similar trends of C_D^{volume} and C_L^{volume} are found for more dimensions. The lowest drag coefficient C_D^{volume} and highest lift coefficient C_L^{volume} are observed for the trapezoidal-type geometry with the highest CWR. For such cases, the geometry design should be such that it has the minimum drag coefficient C_D^{volume} while maximizing the lift coefficient C_L^{volume} in the comparison of different geometries. This design depends on the pattern of vortices formed and shedding from different geometries, which will be discussed in the following section.

4.4 Flow domain and vortex

To investigate the wave dissipation and energy capture characteristics in the interaction of waves with FB-WEC structures, the flow field domain and vortex evolution are discussed in this section. According to the above discussion,

Table 6 Corresponding wave period of the highest heave motion and CWR for different structure dimensions

Structure type	(D, V) (m, m^3)	Natural period T_n^*	Highest heave period $T^*_{\zeta\max}$	Highest CWR period $T^*_{\eta e\max}$
Trapezoidal type (D_0, V_1)	(0.15, 0.0978)	0.22	0.21	0.21
L type (D_0, V_0)	(0.15, 0.0565)	0.20	0.17	0.21
L type (D_3, V_3)	(0.10, 0.0470)	0.19	0.21	0.21
L type (D_2, V_2)	(0.25, 0.0755)	0.22	0.21	0.21
L type (D_1, V_1)	(0.36, 0.0978)	0.24	0.24	0.24

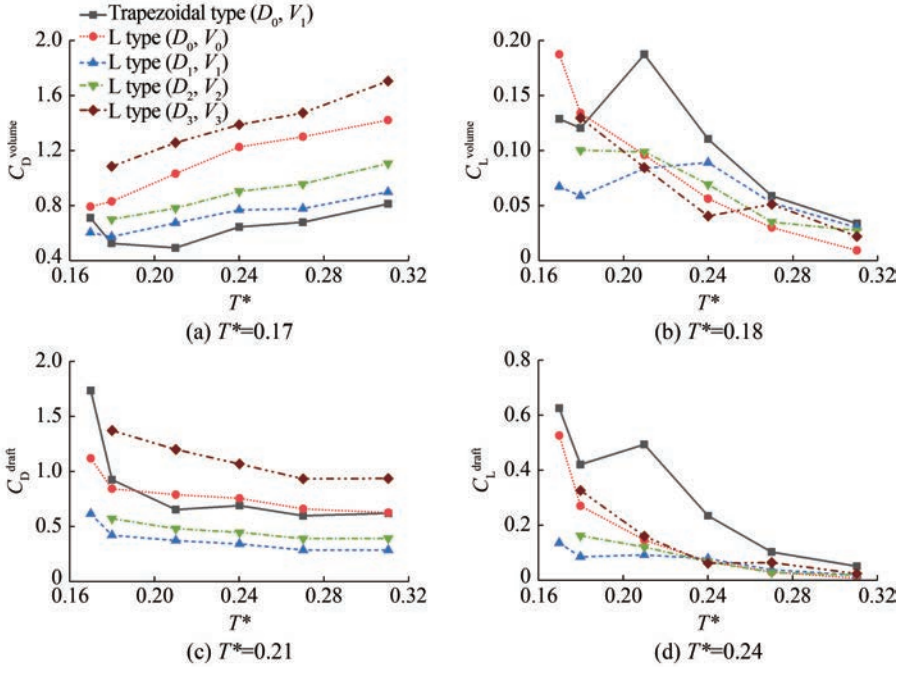

Figure 19 Force coefficients with the variation in wave periods for different dimensions

the best performances of the two types, $T^* = 0.21$ and $B_{PTO} = 100$ kg/s for the trapezoidal type of (D_0, V_1) and $T^* = 0.18$ and $B_{PTO} = 150$ kg/s for the L type of (D_0, V_0), are chosen. The vorticity and velocity fields at four moments of an entire period are shown in Figures 20–21 and Figures 22–23, respectively. In the vorticity figures, the negative vorticity has a clockwise circulation, and the positive vorticity has a counterclockwise circulation.

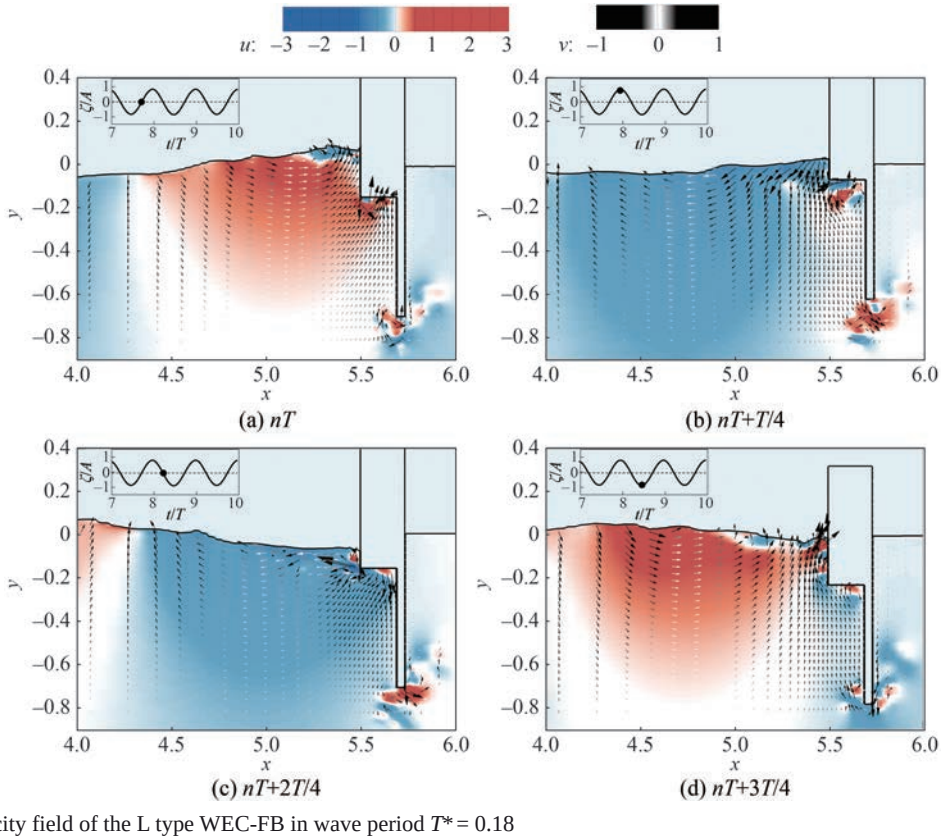

Figure 20 U velocity field of the L type WEC-FB in wave period $T^* = 0.18$

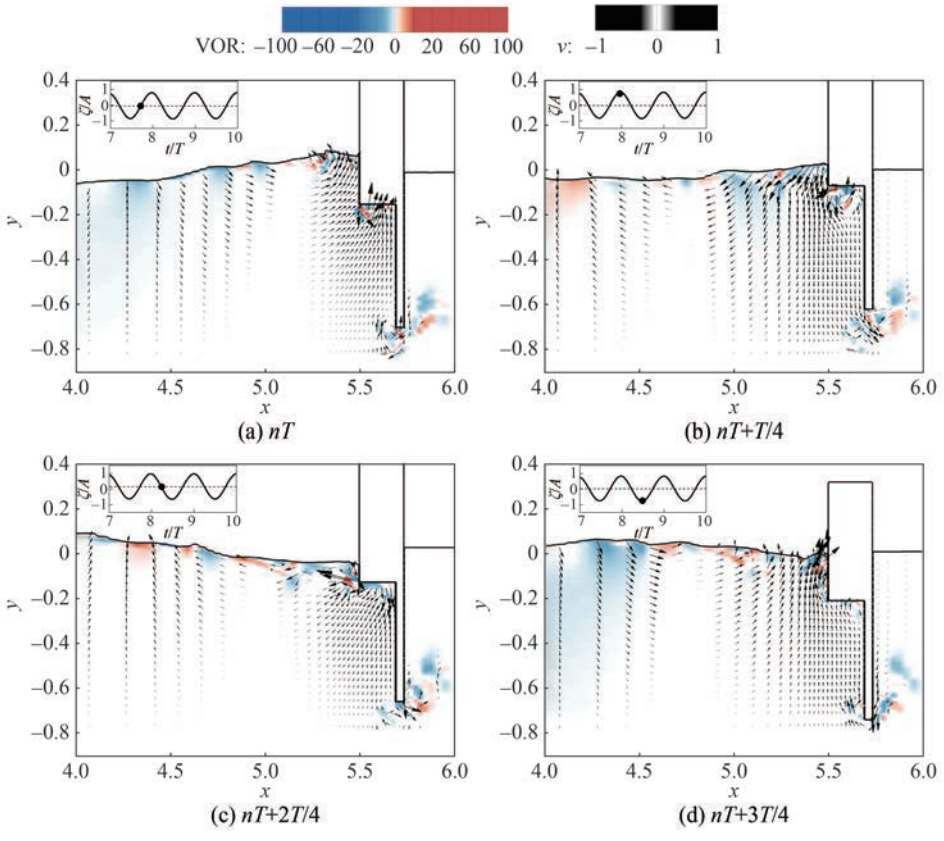

Figure 21 Vorticity and *v* velocity field of the L type WEC-FB in wave period $T^* = 0.18$

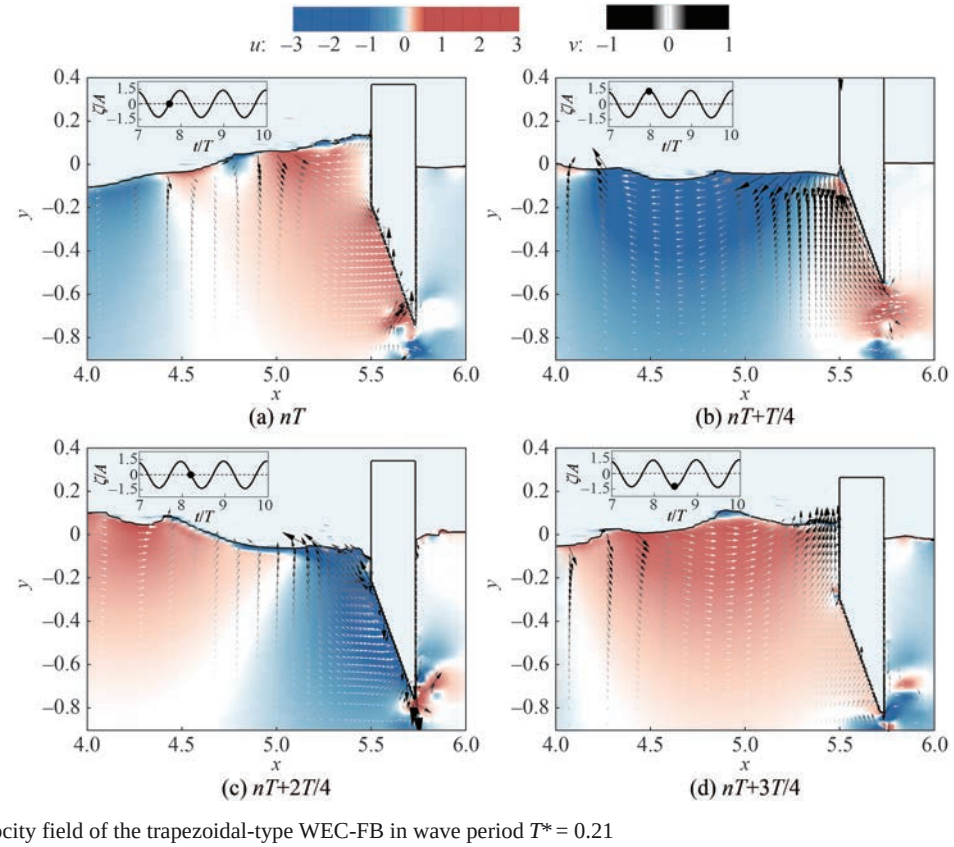

Figure 22 *U* velocity field of the trapezoidal-type WEC-FB in wave period $T^* = 0.21$

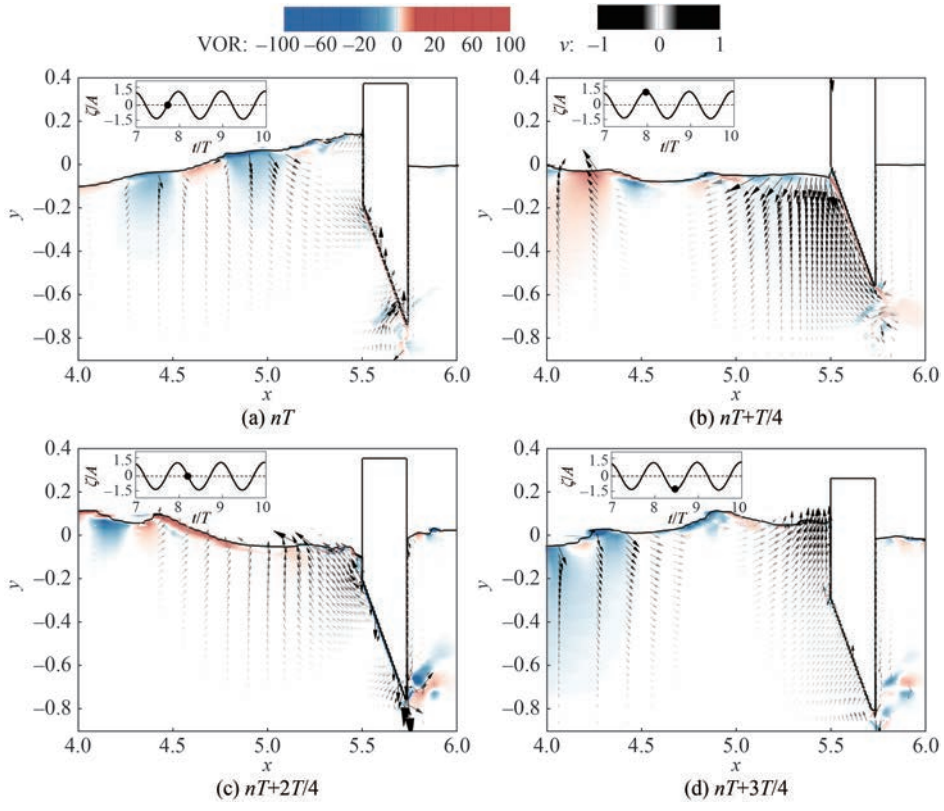

Figure 23 Vorticity and *v* velocity field of the trapezoidal-type WEC-FB in wave period $T^* = 0.21$

In Figure 20(a), as the floater is moving upward from its normal position, flow separations are generated at the corners of the box and wave baffle and grow stronger, and two strong counterclockwise vortices are observed in the left-hand corners of the box and wave baffle in Figure 21(a). At the same time, a small clockwise vortex is created on the right-hand side of the wave baffle. As the floater rises to the top, the two counterclockwise flow separations at the corners propagate downstream under the bottom of the box and the wave baffle in Figures 20(b), and vortex shedding occurs in Figure 21(b). In Figures 20(c)–20(d) and Figures 21(c)–21(d), flow separation and turbulence occur similarly in opposite directions. From Figure 20(b) to Figure 20(c), we see that the flow before the wave baffle is separated into two dimensions, one with a negative *u* velocity that propagates backward as a reflection, the other passing over the wave baffle as a diffraction. This finding explains the large reflection coefficient of the L type.

In Figures 22 and 23, similar flow separations and vortices are observed at the bottom tip of the triangle, but no separation clearly occurs along the left edge of the floater because the boundary layer separation is suppressed by the smoother shape of the triangle. Thus, less turbulent energy is dissipated and more incident wave energy is captured by the PTO system, leading to a higher heave motion and better energy capture performance than the L-shaped floater.

5 Conclusions

In this paper, two WEC-FB structures combining a wave energy converter into an asymmetric floating breakwater have been investigated and compared numerically at the operational mode in terms of their hydrodynamic properties. The WEC-FB comprises a floating square box and an additional structure attached to its rear side, one a triangular structure referred to as trapezoidal type, the other a wave baffle structure referred to as L type. It is moored by a vertical pile, thus responding merely in heave, and a linear damping PTO system is set to simulate the WEC. Four wave periods and one wave height are selected to represent the operational wave conditions of the WEC-FB. The influence of the PTO damping coefficient is illustrated in each wave period. The relation between the optimum hydrodynamic performance and the wave period is explored and studied for both structural types. In addition, for a better understanding of the effect of structural geometry on the hydrodynamic performance, two basic dimensions, one with the same box draft and the other with the same displacement, are discussed. To gain a thorough understanding, the fluid domain and vortices are analyzed and compared between the two floater geometries. The following conclusions can be drawn from this study:

The PTO damping considerably influences the wave

energy CWR and transmission coefficient. In each wave period, the CWR shows an increasing trend and then a decreasing trend with increasing PTO damping.

The optimal PTO damping coefficient B_{oPTO} decreases and then increases with increasing wave period, and the trapezoidal type has the smallest B_{oPTO} among three dimensions in each wave period, implying that its radiation damping is the lowest.

The transmission coefficient shows a decreasing trend in a wave period shorter than the natural period ($T^* < T_n^*$) and an increasing trend in a wave period longer than the natural period ($T^* > T_n^*$).

For both structural types, the highest CWR is achieved in the wave period near the natural period of the WEC-FB, and the resonance between the incident wave and the WEC-FB is verified by analyzing heave motions.

In the range of all studied wave periods, the trapezoidal type has the highest CWR among all the dimensions of the two types.

Given the same box draft of the two types, the trapezoidal type outperforms the L type in terms of energy capture width ratio at $T^* = 0.21–0.27$. At some shorter wave periods $T^* = 0.17–0.18$, the L type shows better wave energy conversion ability than the trapezoidal type. Moreover, the L type has a smaller displacement volume, making it less expensive to manufacture and install.

For the L type, with a decrease in box draft or displacement volume, the wave power capturing performance increases, while the wave protection effect decreases slightly, regardless of the incident wave periods.

Given the same draft of the floater, the drag and lift coefficients influenced by the displacement volume can be considered an appropriate criterion for choosing a suitable geometry for the buoy by minimizing drag coefficient C_D^{volume} and maximizing lift coefficient C_L^{volume}.

Given one geometry type, the drag and lift coefficients influenced by the box draft may be effective for a parameter optimization in draft by maximizing the drag coefficient C_D^{draft} and lift coefficient C_L^{draft}.

The comparisons of flow domain and vortices for both types verified that a triangular shape reduces the vortex generation at the corner of the box, and thus less energy is dissipated and more energy is captured.

The results of this study show that two types of structures provide guidance in terms of hydrodynamic performance for the practical engineering design of the modified geometric shape of the WEC-FB. The technology developers should determine the optimum trade-off design by considering the hydrodynamic performance and the consequent manufacturing cost.

Funding Supported by Shandong Provincial Natural Science Foundation, China (ZR2020ME259), and Open Fund of Shandong Key Laboratory of Civil Engineering Disaster Prevention and Mitigation (CDPM2021KF21).

Competing interest The authors have no competing interests to declare that are relevant to the content of this article.

References

Berenjkoob NM, Ghiasi M, Guedes Soares C (2021) Influence of the shape of a buoy on the efficiency of its dual-motion wave energy conversion. Energy 214: 1-16. DOI: 10.1016/j.energy.2020.118998

Chen Q, Zang J, Birchall J, Ning DZ, Zhao XL, Gao J (2020) On the hydrodynamic performance of a vertical pile-restrained WEC-type floating breakwater. Renew Energy 146: 414-425. DOI: 10.1016/j.renene.2019.06.149

Chen ZH, Ji CY, Guo J (2021) Performance investigation of an integrated device of oscillating buoy wave energy converter and Floating Breakwater. Ship Engineering 43(10): 22-30. DOI: 10.13788/j.cnki.cbgc.2021.10.04

Choi J, Yoon SB (2009) Numerical simulations using momentum source wave-maker applied to RANS equation model. Coastal Engineering 56: 1043-1060. DOI: 10.1016/j.coastaleng.2009.06.009

Deng ZZ, Ren X, Cheng PD (2021) Numerical simulation on the extraction efficiency and hydrodynamic performance of an OWC device with a pitching front-wall. The Ocean Engineering 39(5): 66-77. DOI: 10.16483/j.issn.1005-9865.2021.05.007

Garcia-Teruel A, Forehand DIM (2022) Manufacturability considerations in design optimisation of wave energy converters. Renewable Energy 187: 857-873. DOI: 10.1016/j.renene.2021.12.145

Han Z, Cao FF, Shi HD (2023) Numerical simulation on the energy capture spectrum of heaving buoy wave energy converter. Ocean Engineering 280: 114475. DOI: 10.1016/j.oceaneng.2023.114475

Haren P (1979) Optimal design of Hagen-Cockerall raft. Master thesis, Massachusetts Institute of Technology, Cambridge, 120-121

Hu CH, Kashiwagi M (2004) A CIP-based method for numerical simulations of violent free-surface flows. Journal of Marine Science and Technology 9: 143-157. DOI: 10.1007/s00773-004-0180-z

Huang ST, Shi HD, Dong XC (2019) Capture performance of a multi-freedom wave energy converter with different power take-off systems. China Ocean Engineering 33(3): 288-296. DOI: 10.1007/s13344-019-0028-2

Ji QL, Xu CH, Jiao CS (2021) Numerical investigation on the hydrodynamic performance of a vertical pile-restrained reversed L type floating breakwater integrated with WEC. Ocean Engineering 238: 109635. DOI: 10.1016/j.oceaneng.2021.109635

Jin SY, Patton, RJ, Guo BY (2019) Enhancement of wave energy absorption efficiency via geometry and power take-off damping tuning. Energy 169(2): 819-832. DOI: 10.1016/j.energy.2018.12.074

Korotkin AI (2009) General discussion of body motion in an ideal infinite fluid. In: Added Masses of Ship Structures. Fluid Mechanics and Its Applications, Springer, Dordrecht, 88: 1-20

Koutandos E, Prinos P, Gironella X (2005) Floating breakwaters under regular and irregular wave forcing: reflection and transmission characteristics. Journal of Hydraulic Research 43(2): 174-188. DOI: 10.1080/00221686.2005.9641234

Li MY, Zhao XZ, Ye ZT (2018) Generation of regular and focused waves by using an internal wave maker in a CIP-based model. Ocean Engineering 167: 334-347. DOI: 10.1016/j.oceaneng.2018.08.048

Liu C (2008) Experimental study on pile-restrained pontoon-plates floating breakwater. Master thesis, Dalian University of Technology, Dalian, 47-54

Lopez-Pavon C, Souto-Iglesias A (2015) Hydrodynamic coefficients and pressure loads on heave plates for semi-submersible floating offshore wind turbines: A comparative analysis using large scale models. Renewable Energy 81: 864-881. DOI: 10.1016/j.renene.2015.04.003

Madhi F, Sinclair ME, Yeung RW (2014) The "Berkeley Wedge": an asymmetrical energy-capturing floating breakwater of high performance. Marine Systems & Ocean Technology 9: 5-16. DOI: 10.7666/d.y141723310.1007/bf03449282

Ning DZ, Zhao XL, Göteman M (2016) Hydrodynamic performance of a pile-restrained WEC-type floating breakwater: An experimental study. Renewable Energy 95: 531-541. DOI: 10.1016/j.renene.2016.04.057

Reabroy R, Zheng XB, Zhang L (2019) Hydrodynamic response and power efficiency analysis of heaving wave energy converter integrated with breakwater. Energy Conversion and Management 195: 1174-1186. DOI: 10.1016/j.enconman.2019.05.088

Sarpkaya T, Isaacson M, Wehausen JV (1982) Mechanics of wave forces on offshore structures. American Institute of Physics Conference Series 49(2): 466-467. DOI: 10.1063/1.3530017

Son D, Belissen V, Yeung RW (2016) Performance validation and optimization of a dual coaxial-cylinder ocean-wave energy extractor. Renewable Energy 92(7): 192-201. DOI: 10.1016/j.renene.2016.01.032

Wan C, Yang C, Bai XD, Bi CW (2023) Numerical investigation on the hydrodynamics of a hybrid OWC wave energy converter combining a floating buoy. Ocean Engineering 281: 114818. DOI: 10.1016/j.oceaneng.2023.114818

Xiao F, Honma Y, Kono T (2005) A simple algebraic interface capturing scheme using hyperbolic tangent function. International Journal for Numerical Methods in Fluids 48(9): 1023-1040. DOI: 10.1002/fld.975

Yabe T, Xiao F, Utsumi T (2001) The constrained interpolation profile method for multiphase analysis. Journal of Computational Physics 169: 556-593. DOI: 10.1006/jcph.2000.6625

Yeung RW (1975) A hybrid integral-equation method for time harmonic free-surface flows. Proceedings of the 1st International Conference on Numerical Ship Hydrodynamics, Gaithersburg, 581-607

Yeung RW, Antoine P, Nathan T, Tomasz M (2012) Design, analysis, and evaluation of the UC-Berkeley wave-energy extractor. Journal of Offshore Mechanics & Arctic Engineering 134(2): 46-51. DOI: 10.1115/OMAE2010-20492

Zhang HM, Zhou BZ, Vogel C (2020) Hydrodynamic performance of a floating breakwater as an oscillating-buoy type wave energy converter. Applied Energy 257: 113996. DOI: 10.1016/j.apenergy.2019.113996

Zhang HM, Zhou BZ, Zang J (2021) Effects of narrow gap wave resonance on a dual-floater WEC-breakwater hybrid system. Ocean Engineering 225(31): 108762. DOI: 10.1016/j.oceaneng.2021.108762

Zhang WC, Liu HX, Zhang L (2016) Hydrodynamic analysis and shape optimization for vertical axisymmetric wave energy converters. China Ocean Engineering 30(6): 954-966. DOI: 10.1007/s13344-016-0062-2

Zhao XL, Ning DZ, Zou Q (2019) Hybrid floating breakwater-WEC system: A review. Ocean Engineering 186: 106126. DOI: 10.1016/j.oceaneng.2019.106126

Zhao XZ, Hu CH (2012) Numerical and experimental study on a 2-D floating body under extreme wave conditions. Applied Ocean Research 35: 1-13. DOI: 10.1016/j.apor.2012.01.001

Zhou BZ, Zhang Q, Jin P (2022) Geometric asymmetry in the energy conversion and wave attenuation of a power-take-off-integrated floating breakwater. Ocean Engineering 246: 110576. DOI: 10.1016/j.oceaneng.2022.110576

Zhu X (2006) Application of the CIP method to strongly nonlinear wave-body interaction problems. PhD thesis, Norwegian University of Science and Technology, Trondheim, 43-72